

Automatic Gleason grading of prostate cancer using SLIM and machine learning

Tan H. Nguyen^{a, +}, Shamira Sridharan^{a, +}, Virgilia Marcias^c, Andre K. Balla^c, Minh N. Do^b, Gabriel Popescu^{*a}

^aQuantitative Phase Imaging Laboratory, Beckman Institute for Advanced Science and Technology, Dept. of Electrical and Computer Engineering, Univ. of Illinois at Urbana-Champaign, IL USA 61801.

^bComputational Imaging group, Coordinated Science Laboratory, Dept. of Electrical and Computer Engineering, Univ. of Illinois at Urbana-Champaign, IL USA 61801.

^cDept. of Pathology, Univ. of Illinois at Chicago, IL USA 60637.

+ denotes these authors have equal contribution.

ABSTRACT

In this paper, we present an updated automatic diagnostic procedure for prostate cancer using quantitative phase imaging (QPI). In a recent report [1], we demonstrated the use of Random Forest for image segmentation on prostate cores imaged using QPI. Based on these label maps, we developed an algorithm to discriminate between regions with Gleason grade 3 and 4 prostate cancer in prostatectomy tissue. The Area-Under-Curve (AUC) of 0.79 for the Receiver Operating Curve (ROC) can be obtained for Gleason grade 4 detection in a binary classification between Grade 3 and Grade 4. Our dataset includes 280 benign cases and 141 malignant cases. We show that textural features in phase maps have strong diagnostic values since they can be used in combination with the label map to detect presence or absence of basal cells, which is a strong indicator for prostate carcinoma. A support vector machine (SVM) classifier trained on this new feature vector can classify cancer/non-cancer with an error rate of 0.23 and an AUC value of 0.83.

Keywords: automatic diagnosis, Quantitative Phase Imaging, spatial light interference microscopy, SLIM, prostate cancer, diagnosis.

1. INTRODUCTION

233,000 cases of prostate cancer diagnosed in 2014 have made it one of the most common type of cancer in men in the US [2]. It accounts for 10% of all cancer related deaths and is the sixth leading cause of cancer death globally. Biopsy evaluation of the prostate is considered the diagnostic gold standard. The tissue is fixed in formalin, followed by embedding in paraffin wax, sectioning, deparafinizing and staining with different dyes to target different components of the biopsies. Using bright field microscopy, a pathologist evaluates the biopsy and assigns a Gleason score based on the Gleason grading system [3]. To produce accurate diagnosis results, around 7-12 biopsies have to be evaluated under 20x and possibly 40x magnification if further inspection is needed. The system is an important step in the diagnostic process since studies have shown a strong correlation between the Gleason score and patients' survival rate. It also helps clinicians determine most suitable treatment strategies. However, the Gleason score can vary depending on pathologists' training and experience. In some cases, consensus among several pathologists is needed to get reliable diagnosis results.

Over the years, various groups have worked on developing automated diagnosis schemes using H&E images to mitigate the effects of observer bias. Some methods e.g. [4], [5], compute diagnostic metrics directly from the H&E images to produce decision without image segmentation. Although these methods are fast, the accuracy is quite low due to the existence of abundant outliers, i.e. feature vectors with little or no diagnostic value. Other approaches first perform image segmentation followed by computation of metrics relevant to diagnosis [6], [7]. Typically, these techniques use the color information from H&E images to produce initial label maps. Geometrical and biological rules are applied to further refine

them. However, variations in imaging conditions, and concentration of the dyes used for staining tissue result in non-uniform images and thus require extra pre-processing of the images. These factors hinder easy translation of research findings into the clinic.

QPI is a relatively new imaging modality and its applications in diagnosis and prognosis are in a nascent stage. Currently, the methods used to perform diagnosis on unstained samples is limited [8-11]. In previous publications [1, 12-14], we showed that quantitative phase imaging of unlabeled tissue samples can be used for diagnosis and prognosis of prostate and breast cancers. The benefit of QPI is three-fold. First, the imaging modalities to measure the sample's refractive index is non-invasive, no staining is required [15-21]. Second, only intrinsic information is extracted and used for the diagnosis. Finally, the information retrieved is immune to changes in imaging conditions, allowing seamless translation across institutions. Machine learning algorithms can learn textural behavior of the tissue in phase images and produce segmentation results with very high accuracy, even for high grade cancer. More interestingly, morphological features calculated from numerically stained maps, e.g. gland's shape, convexity, solidity were shown to have high diagnosis value in separating Gleason Grade 3 and Grade 4 cancers, with good agreement to the consensus diagnosis from a group of pathologist.

We show that a combination of the segmentation map and textural features further expands the capability of QPI to solve the cancer/non-cancer classification problem. This is a challenging task due to the presence of tissue with high-grade prostatic intraepithelial neoplasia (HGPIN). HGPIN is a non-cancerous condition in which the textural features in tissue are similar to that of high-grade cancer e.g. prominent nucleoli. Morphological features from segmentation maps alone do not describe HGPIN very well. The only feature that could be used to detect HGPIN is the thin layer of basal or myoepithelial cells surrounding benign glands, characteristic of HGPIN. Morphological features cannot be used to detect this layer, as contributors with similar signatures are seen in non-basal cell pixels. In this manuscript, we show how we can combine the label maps with texton-based features to quantitatively describe or identify basal cells. When we successfully identify the signature of basal cells, we can solve the problem of distinguishing cancerous tissue from the non-cancerous regions. Our testing set consists of 131 normal cases, 60 HGPIN cases and 29 benign prostatic hyperplasia (BPH) cases, all imaged with the Spatial Light Interferometry Microscopy (SLIM) method. The accuracy of our method is evaluated based on ground truth provided by certified pathologists. The structure of this paper is as follows. In Section 2, we review on the basic of SLIM imaging and image segmentation. Section 3 shows the cancer/non-cancer diagnosis problem. Summary & further work will be given in Section 5.

2. SLIM IMAGING & CORE SEGMENTATION

SLIM [17] is a common-path, white-light phase imaging modality that can measure optical fluctuations across specimens being imaged with high sensitivity. More specifically, it measures the argument of the sample transmission $\phi(\mathbf{r}) = \arg[T(\mathbf{r})]$. This quantity relates to the sample thickness $h(\mathbf{r})$ and its refractive index difference $\Delta n(\mathbf{r})$ following the relation $\phi(\mathbf{r}) = \langle k \rangle h(\mathbf{r}) \Delta n(\mathbf{r})$ where $\langle k \rangle$ is the mean wavenumber. To measure $\phi(\mathbf{r})$, SLIM decouples the total field U_t into a DC component U_o and an AC component U_s such that $U_t(\mathbf{r}) = U_o + U_s(\mathbf{r}) = U_o \{1 + \beta(\mathbf{r}) \exp[i\Delta\phi(\mathbf{r})]\}$ where $\beta(\mathbf{r}) = |U_s(\mathbf{r})|/|U_o|$, $\Delta\phi(\mathbf{r}) = \arg[U_s(\mathbf{r})] - \arg U_o$. Figure 1 (a) shows the optical setup of the SLIM system. The Fourier spectrum of U_o matches the condenser phase annulus while that of AC field occupies the rest of the focal plane. An SLM, placed at the Fourier plane, generates modulating phase rings that match the phase annulus of the condenser. Four different interference patterns are captured by the camera $I(\mathbf{r}; n) = |i^n U_o + U_s(\mathbf{r})|^2$, $n = 0, \dots, 3$. Using these 4 frames and the coherent assumption, $\beta(\mathbf{r}), \Delta(\mathbf{r})$ are solved explicitly and combined to compute the phase of the sample of interest using $\phi(\mathbf{r}) = \tan^{-1} \left(\beta(\mathbf{r}) \sin[\Delta\phi(\mathbf{r})] / \{1 + \beta(\mathbf{r}) \cos[\Delta\phi(\mathbf{r})]\} \right)$. More details can be found elsewhere [17]. Figure 1 b), c) show H & E and SLIM images of a core from a Tissue Micro-Array (TMA) used in this paper. The whole TMA is shown in Fig. 1 d). This TMA consists of more than 300 tissue cores (1 core per patient). A diagnosis is available for both the specific tissue region sampled in the TMA and the overall prostatectomy tissue, for each patient. A Random Forest classifier is trained to segment the SLIM images into different regions by classifying each pixel into 1 of 3 classes (lumen, gland or stroma). The input feature vectors for the classifier are the histogram of texton-indices surrounding each pixel. Each texton index corresponds to one typical expression of the glandular texture. 50 expressions were learnt from all cores

using K-means clustering on the filter response of the input images to different filter kernels. This feature has been successfully used for various computer vision problems e.g. material classification [22]. The reader is referred to our previous publication [1] for more details.

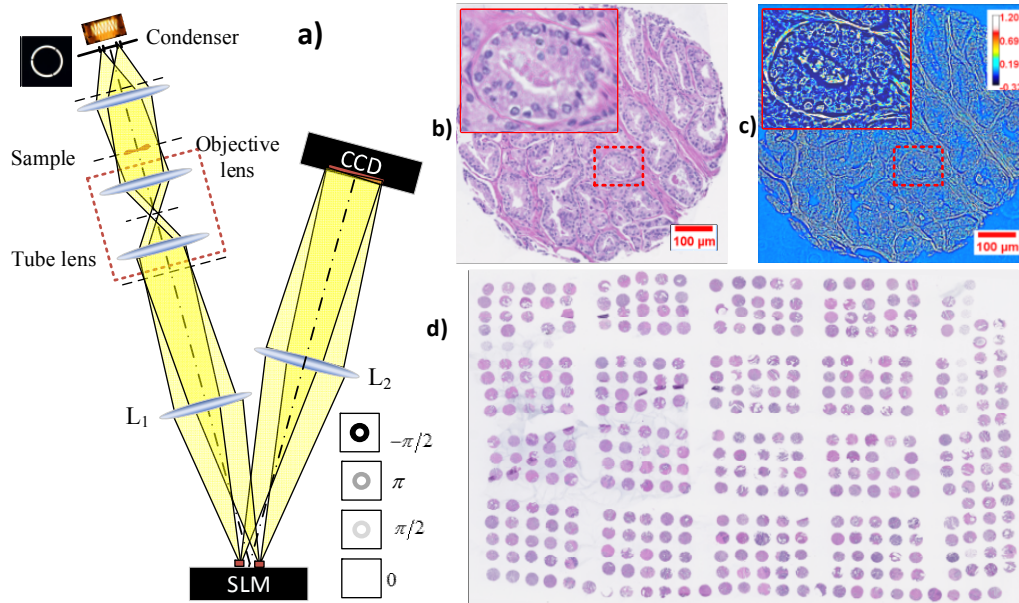


Figure 1. a) Optical setup of SLIM [17], b) c) H & E and SLIM images of a core in the TMA d).

Figure 2 a) shows an H & E image of a Grade 3 core. The automatically segmented map of the core is shown in Fig. 2b) overlaid on the original SLIM map. Here, red corresponds to stromal regions, green corresponds to glandular regions and blue corresponds to luminal regions. The label map has a high degree of correlation with the H & E map. As the cancer progresses to higher grades, more glandular distortions and deformations are observed. Consequently, there is a reduction in segmentation accuracy at higher grades. Fig. 2 c) shows the Receiver's Operating Curve for different diagnosis results. The best performance, i.e., the curve with the highest area under the curve (AUC) is observed for tissue with a diagnosis of BPH (AUC 0.98). Gleason score 10 tissue shows no glandular presence and has individual epithelial cells embedded in stroma. Therefore, it is not surprising that the classifier has the smallest AUC in this group. However, an AUC = 0.87 is still considered to be within a high degree of agreement with the H&E classification. More segmentation results can be found in [1].

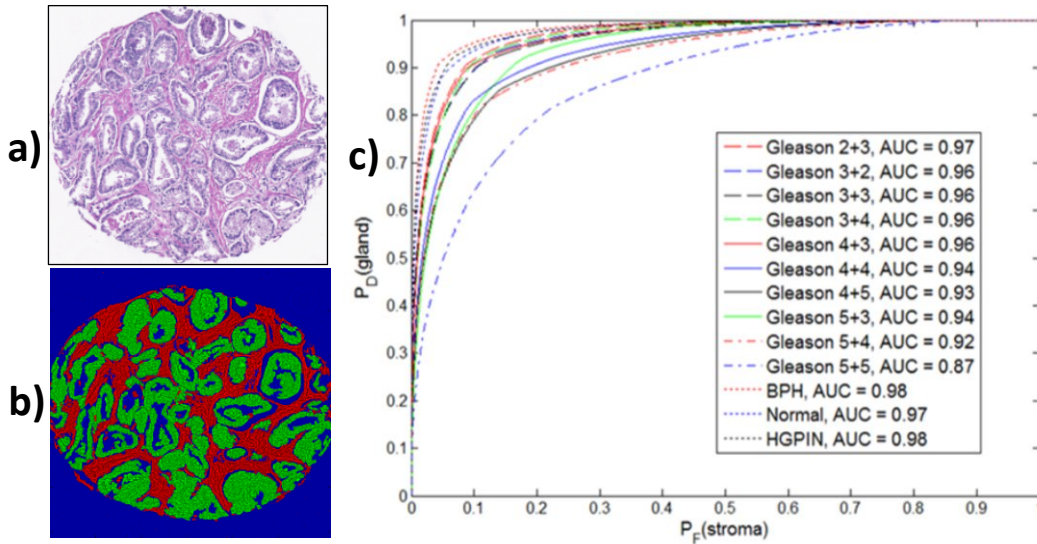


Figure 2. a) H & E stained image of a Gleason grade 3 core, b) Label map overlaid of SLIM image of the core, c) ROC curve for different classes. Can you make c higher resolution?

3. AUTOMATIC DIAGNOSIS USING SEGMENTED RESULTS

Given the label map generated for each core, Ref. [1] reports how differential diagnosis of Grade 3 and Grade 4 prostate adenocarcinoma can be obtained using morphological features computed on each glands. Diagnosis result for the whole core can be obtained from those of individual glands using the Bag-of-Words model [23]. However, previous morphological features did not capture the presence of basal cells, which would exclude a diagnosis of carcinoma. Here, we extend the previous diagnostic framework, as shown in Fig. 3.

Candidate regions for basal cells, which is the region at the edge of glands and adjacent to stroma, are identified from the label maps (Diagnosis path in Fig. 3). Subsequently, histograms of texton indices are computed for these candidate regions (one histogram per gland). This refining scheme will significantly reduce the number of pixels interrogated to streamline diagnosis, while also increasing the specificity of feature vectors.

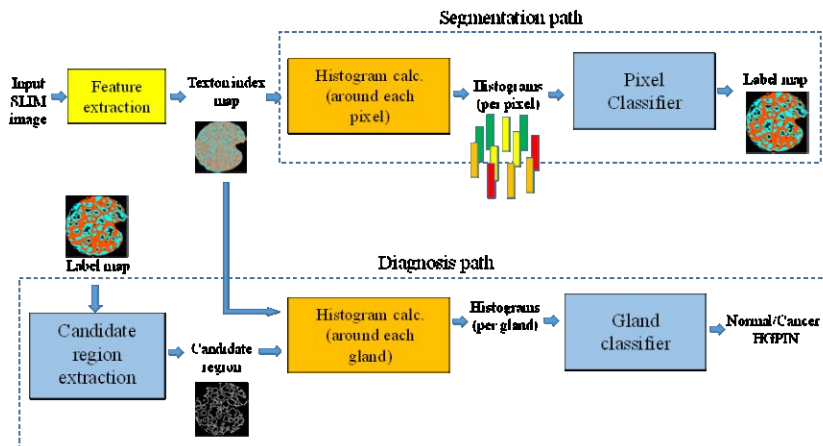


Figure 3. How diagnosis is done to determine the existence of prostate cancer

The feature vectors computed from the new scheme are combined with the pathologists' diagnosis of the core to train a support vector machine (SVM) classifier with a radial basis function kernel. Our data set has 280 cores with cancer and 141 non-cancerous cores. The cores with cancer were sub-classified into Gleason grades 3 and 4. The non-cancerous cores were sub-classified as normal, BPH and HGPIN. A 10-fold cross validation of the new diagnostic scheme was performed on this data set. Our diagnostic results have an AUC of 0.83 with average error of 23%.

4. SUMMARY & FUTURE WORK

This paper extends our previous work on automated diagnosis of prostate cancer. The label map from automatic segmentation is used in a feedback mechanism to identify areas where basal cells are typically located. A classifier is trained to discriminate the textural features in these localized regions in order to determine if the gland is benign or malignant. Further efforts will be focused on improving the accuracy of this method by extending the training set and using multi-scale feature extraction.

5. ACKNOWLEDGMENTS.

This work was supported by the National Science Foundation (CBET-1040461, IIP-1353368) and Agilent Laboratories. For more information, visit <http://light.ece.illinois.edu>

REFERENCES

- [1] T. H. Nguyen, S. Sridharan, V. Macias *et al.*, "Prostate cancer diagnosis using quantitative phase imaging and machine learning algorithms." 933619-933619-10.
- [2] U. C. S. W. Group, "United States cancer statistics: 1999–2010 incidence and mortality web-based report," Atlanta, GA, (2013).
- [3] D. F. Gleason, and E. M. Tannenbaum, "The veteran's administration cooperative urologic research group: Histologic grading and clinical staging of prostatic carcinoma," *Urologic Pathology: The Prostate*, 171-198 (1977).
- [4] J. Diamond, N. H. Anderson, P. H. Bartels *et al.*, "The use of morphological characteristics and texture analysis in the identification of tissue composition in prostatic neoplasia," *Human Pathology*, 35(9), 1121-1131 (2004).
- [5] R. Farjam, H. Soltanian-Zadeh, R. A. Zoroofi *et al.*, "Tree-structured grading of pathological images of prostate." 840-851.
- [6] S. Naik, S. Doyle, M. Feldman *et al.*, "Gland segmentation and computerized gleason grading of prostate histology by integrating low-, high-level and domain specific information."
- [7] K. Nguyen, B. Sabata, and A. K. Jain, "Prostate cancer grading: Gland segmentation and structural features," *Pattern Recognition Letters*, 33(7), 951-961 (2012).
- [8] S. Uttam, H. V. Pham, J. LaFace *et al.*, "Early Prediction of Cancer Progression by Depth-Resolved Nanoscale Mapping of Nuclear Architecture from Unstained Tissue Specimens," *Cancer research*, 75(22), 4718-4727 (2015).

- [9] P. Wang, R. Bista, R. Bhargava *et al.*, "Spatial-domain low-coherence quantitative phase microscopy for cancer diagnosis," *Optics letters*, 35(17), 2840-2842 (2010).
- [10] P. Wang, R. K. Bista, W. E. Khalbuss *et al.*, "Nanoscale nuclear architecture for cancer diagnosis beyond pathology via spatial-domain low-coherence quantitative phase microscopy," *Journal of biomedical optics*, 15(6), 066028-066028-8 (2010).
- [11] D. A. Brokl, D. Y. Lo, W. E. Khalbuss *et al.*, "Spatial-domain low-coherence quantitative phase microscopy to improve the cytological diagnosis of pancreatic cancer," *Gastroenterology*, 140(5), S-53 (2011).
- [12] Z. Wang, K. Tangella, A. Balla *et al.*, "Tissue refractive index as marker of disease," *J. Biomed. Opt.*, 16(11), (2011).
- [13] S. Sridharan, V. Macias, K. Tangella *et al.*, "Prediction of Prostate Cancer Recurrence Using Quantitative Phase Imaging," *Scientific reports*, 5, (2015).
- [14] H. Majeed, M. E. Kandel, K. Han *et al.*, "Breast cancer diagnosis using spatial light interference microscopy," *Journal of biomedical optics*, 20(11), 111210-111210 (2015).
- [15] G. Popescu, [Quantitative Phase Imaging of Cells and Tissues] McGraw-Hill, (2011).
- [16] T. H. Nguyen, and G. Popescu, "Spatial Light Interference Microscopy (SLIM) using twisted-nematic liquid-crystal modulation," *Biomedical optics express*, 4(9), 1571-1583 (2013).
- [17] Z. Wang, L. J. Millet, M. Mir *et al.*, "Spatial light interference microscopy (SLIM)," *Opt. Exp.*, 19(1016), (2011).
- [18] B. Bhaduri, C. Edwards, H. Pham *et al.*, "Diffraction phase microscopy: principles and applications in materials and life sciences," *Advances in Optics and Photonics*, 6(1), 57-119 (2014).
- [19] G. Popescu, T. Ikeda, R. R. Dasari *et al.*, "Diffraction phase microscopy for quantifying cell structure and dynamics," *Opt. Lett.*, 31(6), 775-777 (2006).
- [20] E. Cuhe, F. Bevilacqua, and C. Depeursinge, "Digital holography for quantitative phase-contrast imaging," *Opt. Lett.*, 24(5), 291-293 (1999).
- [21] P. Bon, G. Maucort, B. Wattellier *et al.*, "Quadriwave lateral shearing interferometry for quantitative phase microscopy of living cells," *Opt. Express*, 17(15), 13080-13094 (2009).
- [22] M. Varma, and A. Zisserman, [Classifying images of materials: Achieving viewpoint and illumination independence] Springer, (2002).
- [23] L. Fei-Fei, and P. Perona, "A bayesian hierarchical model for learning natural scene categories." 2, 524-531.